Mirror Surface Reconstruction Using Polarization Field

Jie Lu[1,3], Yu Ji[2], Jingyi Yu[1,2], and Jinwei Ye[3]
[1]ShanghaiTech University, Shanghai, 201210 China
[2]DGene Inc., Baton Rouge, LA 70820 USA
[3]Louisiana State University, Baton Rouge, LA 70803 USA

Mirror surfaces are notoriously difficult to reconstruct. In this paper, we present a novel computational imaging approach for reconstructing complex mirror surfaces using a dense illumination field with angularly varying polarization states, which we call the *polarization field*. Specifically, we generate the polarization field using a commercial LCD with the top polarizer removed. We mathematically model the liquid crystals as polarization rotators using Jones calculus and show that the rotated polarization states of outgoing rays encode angular information (e.g., ray directions). To model reflection under the polarization field, we derive a reflection image formation model based on the Fresnel's equations and estimate incident ray positions and directions by coding the polarization field. Finally, we triangulate the incident rays with the camera rays to recover normals/depths of the mirror surface. Comprehensive simulations and real experiments demonstrate the effectiveness of our approach.

***Index Terms*—polarization, liquid crystal display, 3D reconstruction, mirror surface**

I. Introduction

Mirror surfaces are difficult to reconstruct as their appearances are borrowed from surrounding environment and thereby can be regarded as "invisible". Most well-established 3D reconstruction techniques (e.g., multi-view stereo, shape from shading, structured light, etc.) are not directly applicable to this task. However, successful reconstruction can benefit many applications, such as manufacturing, material inspection, robotics, art digitalization and preservation, etc.

Existing solutions for mirror surface reconstruction often place an illuminant with known pattern near the mirror surface and use a camera looking towards the surface to capture the reflection images. By analyzing the correspondences between the reflection image and the known pattern, ray paths from the illuminant to the camera are triangulated to recover the surface geometry (e.g., depth or normal field). However, correspondences between image pixels and pattern points are under-constrained since knowing a point on a ray is insufficient to determine its path: the ray's direction also needs to be known. In order to determine the ray direction, existing solutions use multiple viewpoints [1]–[3] or a moving illuminant [4] to acquire multiple points on the path. Otherwise, additional geometry constraints such as planarity assumption [5], smoothness prior [6], and surface integrability constraint [7] need to be assumed.

In this paper, we present a novel computational imaging approach for reconstructing complex mirror surfaces using a pair of LCD and viewing camera (see Fig. 1). We exploit the polarization rotation properties of liquid crystals and remove the top polarizer of an LCD to create polarization field, in which each outgoing ray has a unique polarization state. Lanman *et al.* [8] stack multiple liquid crystal layers and use the polarization field to implement autostereoscopic display that produce view-dependent images. We, instead, take advantage of the angular information embedded in the polarization field for reconstructing mirror surfaces. To characterize the polarization states with respect to ray directions, we model the polarization rotation induced by liquid crystals using Jones calculus and show that the outgoing rays are elliptically polarized when voltage applied to the liquid crystals. In particular, the ellipse's orientation (i.e., directions of major and minor axes) is associated with ray direction and the ellipticity (i.e., ratio between major and minor axes) depends on the applied voltage (or the input intensity to LCD). Since polarized light has different reflection rate when interacts with the mirror surface, the polarization field exhibits various intensities in the reflection image. To model reflection under the polarization field, we derive a reflection image formation model using Fresnel's equations that describe the reflection and transmission of light as electromagnetic wave when incident on an interface between different media. We then optimize the incident ray

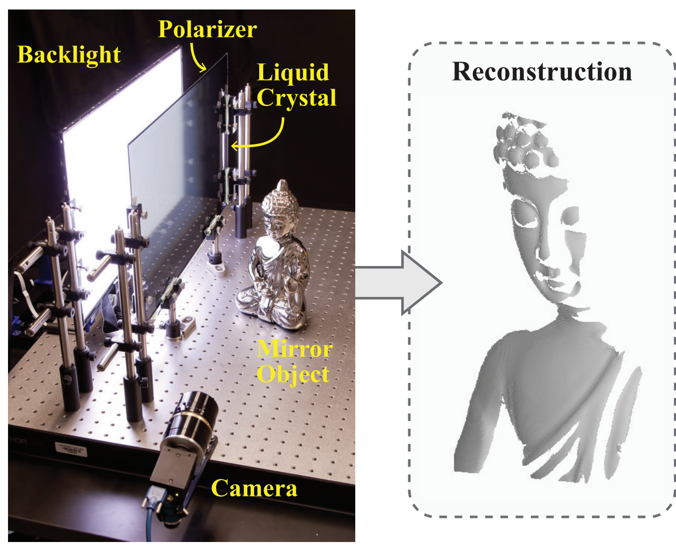

Fig. 1. Left: our experimental setup for mirror surface reconstruction that uses a commercial LCD (top polarizer removed) to generate the polarization field; Right: reconstructed mirror surface with our approach.

Corresponding author: Jinwei Ye (email: jye@csc.lsu.edu). This work was performed when Jie Lu was a visiting student at LSU.

directions from the captured reflection images. As we consider combined intensity for polarized light in our reflection image model, we eliminate the use of a rotating polarizer during acquisition. To estimate the incident rays, we first decode their positions using Gray Code and then optimize their directions by applying our reflection image model. Finally, we triangulate the incident rays and camera rays to obtain the surface normals and recover the 3D surface by Poisson integration. We perform comprehensive experiments on both simulated and real surfaces to demonstrate that our approach is able to recover a broad range of complex surfaces with high fidelity.

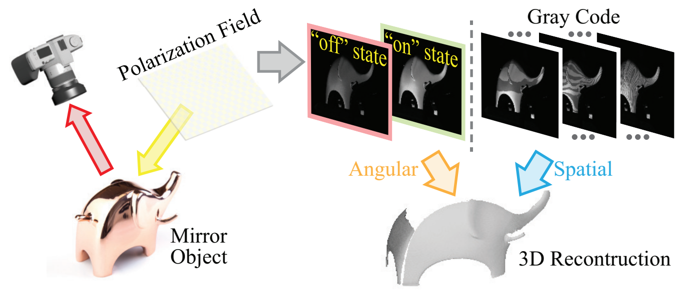

Fig. 2. Overview of our mirror surface reconstruction approach using polarization field.

II. Related Work

In this section, we briefly review existing methods for mirror or specular surface reconstruction. Early approaches investigate distortions in reflection images for recovering the shape of specular objects. Conceptually, specular distortions are combined results of the specular object geometry and the surrounding environment. Given a known pattern in the environment, the object shape can be inferred consequently. Psychophysic studies [9], [10] indicate that specular distortion is an important visual cue for human vision to perceive the shape of a specular object. In computer vision, various patterns, such as grids [11], checkers [6], stripes [7], and lines [12], [13] are adopted for studying the specular distortion. Caustic distortion caused by mirror reflection is examined for geometry inference in [14]. Although local surface geometry properties such as orientations and curvatures can be recovered from specular distortions, the overall 3D geometric model still remains ambiguous (e.g., the concave vs. convex ambiguity) and additional surface constraints such as near-flat surface [13] and integrability [7] need to be applied to resolve ambiguities. In our approach, no geometric constraints need to be imposed on the surface shape.

Some approaches exploit the motion of specular reflections, or specular flow, for shape reconstruction. Usually, the specular flow is generated by a moving light source [15] or camera [16]. Alternatively, an array of cameras [17] or light sources [5], [18] can be used. Then feature correspondences among the specular flow are analyzed for 3D reconstruction. Instead of using a spotlight, [19]–[21] use features in uncontrolled environment for estimating the specular flow. [22] generalizes invariant features in specular reflection for correspondence matching. [23] uses the specular flow to refine a rough geometry obtained from space carving. This class of approaches usually rely on a know motion of the object, the environment, or the camera respectively. Furthermore, due to the reflection distortions, it is non-trivial to observe dense specular flow. [21] proposes sparse specular flow but the reconstructed surface is assumed quadratic. Therefore, this class of methods are not suitable to handle objects with complex shapes that cause severe distorted reflections. Our approach is able to handle a broad range of mirror surfaces with complex shapes, including both convex and concave (as long as no inter-reflection occurs).

Another class of approaches directly recover the incident and reflected rays on the specular surface and use ray-ray triangulation to recover the 3D geometry. Often coded patterns (e.g., the Gray Code [3], [24] or phase shifting patterns [1], [2]) are laid out on the mirror surface. By establishing correspondences between image pixels and pattern points, the surface is reconstructed by triangulating the incident rays with reflected rays. Since a ray is uniquely determined by at least two points, multiple viewpoints [1]–[3], [25] or a moving pattern [4], [26]–[28] are commonly used to locate multiple points on the ray path. Some approaches use additional constraints, such as radiometric cues [29] or frequency domain correspondences [30] to determine the incident ray from one point on the path. In our approach, incident rays are solved from the angular information encoded in the polarization field.

Shape from polarization is a popular class of 3D reconstruction techniques that estimates surface shape from the polarization state of reflected light. In a common setup, a polarizer is mounted in front of the camera and multiple images are captured under different polarization angles. Then by fitting the phase function with captured intensities, the azimuth angle of surface normal can be estimated. However, due to symmetry of the cosine function, the azimuth angle has the π-ambiguity: flipping the surface by π results in the same polarization measurements. To resolve this ambiguity, additional assumptions, such as shape convexity [31], [32] and boundary normal prior [33] need to be made. Some approaches combine the polarization cue with other photometric cues, such as shape-from-shading [34], [35], photometric stereo [36], [37], or multi-spectral measurements [38] to disambiguate the normal estimation. Recent trend is to use shape from polarization to recover fine details on top of a coarse geometry. Multi-view stereo [39]–[41], space carving [42], structure from motion [43] or RGB-D sensors [44] can be used to initiate the coarse geometry. In our approach, we exploit the polarization states of illumination source. As we consider the combine intensity when forming the reflection image, we do not need to use a rotating polarizer on the acquisition camera and our normal estimation is free from the π-ambiguity.

III. Overview

Fig. 2 shows an overview of the proposed mirror surface reconstruction approach using polarization field. We remove the top polarizer of an LCD to generate the polarization field that illuminate the mirror surface. A camera captures the reflection images under the polarization field. It is worth noting that the acquisition camera does not need to use a rotating polarizer as we consider combined intensity in our reflection image model. We display a sequence of Gray Code images, including all black (i.e., "off" state) and all white (i.e., "on" state) for estimating the incident rays. We first decode the Gray code to obtain originating LCD pixels for each captured incident ray and then optimize the ray directions by applying our reflection image formation model that characterize reflected intensities for different polarization states. Finally, we triangulate the incident rays and camera rays to obtain the surface normals and recover the 3D surface by Poisson integration.

IV. Polarization Field

This section describes how to generate the polarization field with a commercial LCD. First, we review the working principles of LCDs and model the polarization of outgoing rays using Jones calculus. We then analyze the polarization with respect to the outgoing ray directions and show that the polarization states encode angular information.

A. LCD polarization analysis

A liquid crystal display (LCD) is composed of a uniform backlight and a liquid crystal layer controlled by electrodes and sandwiched between two crossed linear polarizers [45]. By controlling the voltage applied across the liquid crystal layer in each pixel, the liquid crystals alter orientations and rotate the polarization of outgoing rays. This results in varying amount of light to pass through the polarizer and thus constitute different levels of gray. Since the top polarizer regulates the polarization states to align with itself, we remove the top polarizer to allow the outgoing rays to carry different polarization states modulated by the liquid crystals and thus generate the polarization field. In our experiment, we use a normal black (NB) in-plane switch (IPS) LCD, in which the liquid crystals are homogeneous and rotated in multiple transverse planes.

Fig. 3 shows how the liquid crystals in an NB IPS device alters polarization states of outgoing rays with/without voltage applied. The unpolarized light emitted from the uniform backlight is first linearly polarized. After modulated by the liquid crystal, the light may exhibit two different types of polarization: linear or elliptical. When no voltage is applied, the liquid crystals are all aligned with the first polarizer (vertical). As result, the polarization states of light passing through is not rotated and remain linearly polarized (aligned with the first polarizer). When voltage of the electrodes is on, the liquid crystals rotate in plane as response and cause polarization rotation for light passing through. In the following, we show that the outgoing rays are generally elliptically polarized and the ellipse's orientation is related to the ray direction.

We use the Jones calculus to mathematically characterize the polarization states of outgoing rays emitted from the polarization field. In Jones calculus, polarized light is represented by Jones vector in terms of its complex amplitude and linear optical elements are represented 2×2 Jones matrices. When light crosses an optical element, the resulting polarization of emerging light is found by taking the product of the Jones

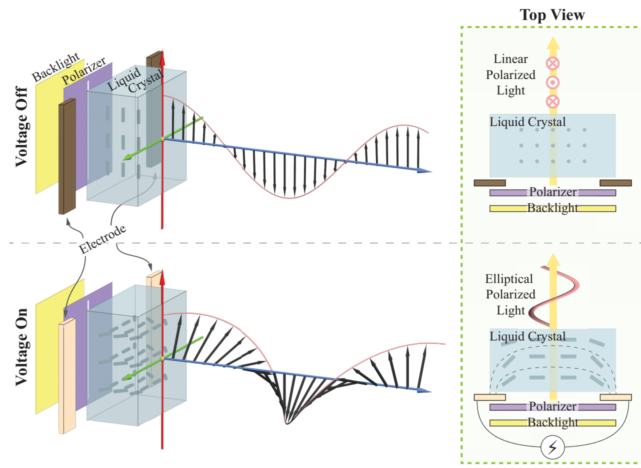

Fig. 3. Liquid crystals rotate the polarization state of light passing through when voltage applied.

matrix of the optical element and the Jones vector of the incident light.

We set up our coordinate on the display plane as shown in Fig. 4. The unpolarized backlight first passes through the polarizer and becomes linearly polarized. In terms of Jones vector, the polarization of the linearly polarized light can be written as:

$$V = \begin{bmatrix} V_x \\ V_y \end{bmatrix} = \begin{bmatrix} \cos\omega \\ \sin\omega \end{bmatrix} \tag{1}$$

where ω defines the orientation of the linear polarizer. For a vertical polarizer, $\omega = \pi/2$.

When voltage is applied on the electrodes, the liquid crystals within a cell rotates on multiple transverse planes in the IPS mode. Assume a cell is decomposed into N transverse planes with in-plane rotated liquid crystals. Each plane can be considered as a homogeneous wave plate since the liquid crystals rotate uniformly and the Jones matrix can be written as:

$$W_i(\Psi_i) = \begin{bmatrix} e^{-\frac{i\pi}{2N}} \cos^2\Psi_i + e^{\frac{i\pi}{2N}} \sin^2\Psi_i & -i\sin(\frac{\pi}{2N})\sin(2\Psi_i) \\ -i\sin(\frac{\pi}{2N})\sin(2\Psi_i) & e^{-\frac{i\pi}{2N}} \sin^2\Psi_i + e^{\frac{i\pi}{2N}} \cos^2\Psi_i \end{bmatrix} \tag{2}$$

where $i \in [1, N]$ is the index of transverse plane and Ψ_i is the angle of rotation for liquid crystals on the i^{th} plane.

By multiplying the Jones matrices (Eq. 2). of all transverse planes with the Jones vector of the linearly polarized light (Eq. 1), we obtain the polarization of the emitted light as:

$$V' = \prod_{i=1}^{N} W_i(\Psi_i) V \tag{3}$$

Since V' is composed complex numbers, the outgoing rays are elliptically polarized and the polarization state is determined by the applied voltage (or the input intensity to LCD) and the ray direction. Specifically, the voltage defines the ellipticity (i.e., ratio between major and minor axes) and

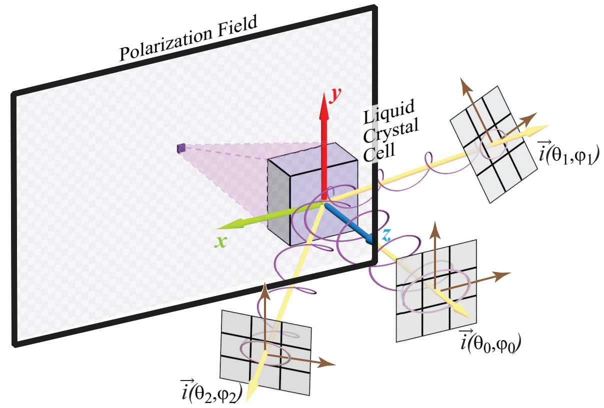

Fig. 4. Outgoing rays from the polarization field are elliptically polarized. The ellipse's orientation is associated with the propagation direction.

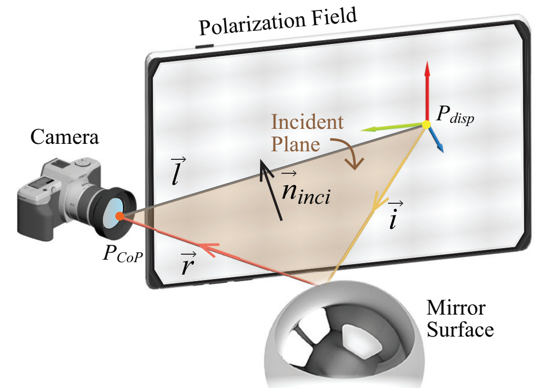

Fig. 5. Incident plane of reflection (formed by the incident ray and the reflected ray).

the outgoing ray direction determines the ellipse's orientation (i.e., directions of major and minor axes) because the voltage controls the rotation angle of liquid crystals (i.e., Ψ_i) and the ellipse plane is normal to the ray propagation direction.

B. Angularly varying polarization states

Next, we characterize polarization states of outgoing rays with respect to their propagation directions. Since an elliptically polarized wave can be resolved into two linearly polarized waves along two orthogonal axes, we set out to find the major and minor axes of the ellipse and decompose the emitted light onto the two axes.

Given an outgoing ray emitted from the the polarization field as $\vec{i}(\theta,\phi)$, where θ and ϕ are the zenith and azimuth angles. Since the elliptical plane is normal to the ray's propagation direction (see Fig. 4), we can formulate the two orthogonal axes by cross product:

$$\begin{aligned} \vec{d_1} &= \frac{\vec{y} \times \vec{i}(\theta,\phi)}{\| \vec{y} \times \vec{i}(\theta,\phi) \|} \\ \vec{d_2} &= \frac{\vec{d_1} \times \vec{i}(\theta,\phi)}{\| \vec{d_1} \times \vec{i}(\theta,\phi) \|} \end{aligned} \tag{4}$$

where $\vec{y}$ is the y-axis and $\vec{i}(\theta,\phi)$ is the outgoing ray's propagation direction.

We then decompose the elliptically polarized light along $\vec{i}(\theta,\phi)$ onto $\vec{d_1}$ and $\vec{d_2}$ as $\vec{E}_1$ and $\vec{E}_2$ and define the amplitude ratio γ between the two decomposed waves as:

$$\gamma(\theta,\phi,\nu_k) = \frac{\| \vec{E}_1(\nu_k) \|}{\| \vec{E}_2(\nu_k) \|} = \sqrt{\frac{I_{d_1}(\nu_k)}{I_{d_2}(\nu_k)}} \tag{5}$$

where ν_k ($k = 0, ..., 255$, which refers to the input intensity) is the applied voltage; I_{d_1} and I_{d_2} are captured intensities by applying a polarizer along d_1 and I_{d_2} on the acquisition camera, which models the energy of the decomposed waves.

When the ray is normal to the display plane ($\theta = \phi = 0$), the major and minor axes of the polarization ellipse are aligned with the x-axis and y-axis. The amplitude ratio after decompose can be written as:

$$\gamma(0,0,\nu_k) = \frac{E_{\Leftrightarrow}(\nu_k)}{E_{\Updownarrow}(\nu_k)} = \sqrt{\frac{I_{\Leftrightarrow}(\nu_k)}{I_{\Updownarrow}(\nu_k)}} \tag{6}$$

where $E_{\Leftrightarrow}$ and $E_{\Updownarrow}$ denotes the decomposed waves; $I_{\Leftrightarrow}$ and $I_{\Updownarrow}$ are intensities captured by applying a horizontal and vertical polarizer.

Since the IPS LCD has very wide viewing angle, the amplitude ratios γ are almost the same for different viewing angles. We therefore use $\gamma(0,0,\nu_k)$ to approximate the ratio at arbitrary angles $\gamma(\theta,\phi,\nu_k)$. We also justify this approximation using experiments by capturing polarized intensity ratios from different viewing angles (see Section VI-B). The ratio γ is critical to determine the energy of decomposed waves, this approximation greatly simplifies the procedure for measuring γ: we only need to measure the ratio between the vertical and horizontal polarization images for each intensity level.

Assume the elliptically polarized light energy is normalized to 1, the decomposed waves along d_1 and d_2 for ray $\vec{i}(\theta,\phi)$ can be written as:

$$\begin{aligned} \vec{E}_1(\nu_k) &= \frac{\gamma(0,0,\nu_k)}{1+\gamma(0,0,\nu_k)} \cdot \vec{d_1} \\ \vec{E}_2(\nu_k) &= \frac{1}{1+\gamma(0,0,\nu_k)} \cdot \vec{d_2} \end{aligned} \tag{7}$$

V. Mirror Surface Reconstruction

In this section, we describe how to recover mirror surface using polarization field. We first derive a reflection image formation model under the polarization field since reflection alters the polarization of light. We show that the reflection image is a function of incident ray direction. We therefore optimize the incident ray directions from the captured reflection images. Finally, we triangulate the incident rays with reflected rays for surface reconstruction.

A. Reflection image formation

Assume we have obtained the viewing camera's center of projection (CoP) P_{CoP} and camera rays (or reflected rays) $\vec{r}$ from camera calibration and the pixel-point correspondences

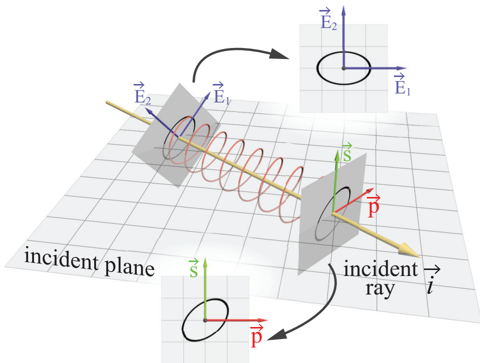

Fig. 6. s- and p-polarization decomposition for an incident ray.

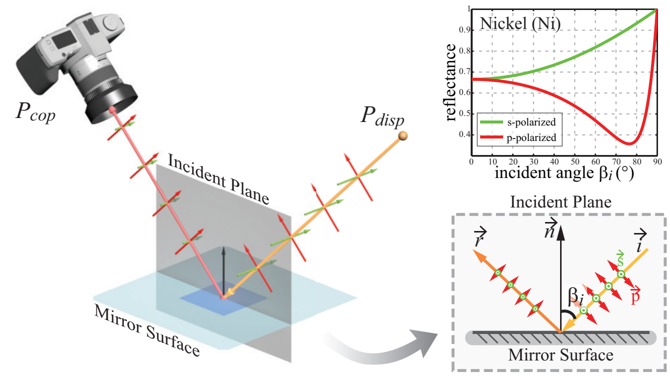

Fig. 7. The reflection rate is related to the polarization states, incident angle, and surface material (i.e., the refractive index). The p-polarized light and s-polarized light has different reflectance coefficients.

(between the captured image and displayed image) using Gray Code. We can form an incident plane of reflection for each display pixel P_{disp} as shown in Fig 5. The normal of the incident plane can be derived as:

$$\vec{n}_{inci} = \frac{\vec{l} \times \vec{r}}{\| \vec{l} \times \vec{r} \|} \tag{8}$$

where $\vec{l} = P_{CoP} - P_{disp}$.

Assume the surface point is at depth d, the surface point P_{inter} can be written as:

$$P_{inter} = P_{CoP} - d \cdot \vec{r} \tag{9}$$

Given P_{inter} and P_{disp}, the incident ray that emitted from the polarization field can be written as:

$$\vec{i} = P_{inter} - P_{disp} \tag{10}$$

Eq. 10 indicates the incident ray is a function of surface depth. According to the reflection law, the incident ray $\vec{i}$ is always lying on the plane of incident. We then decompose the polarization state of $\vec{i}$ into two orthogonal linear polarizations: p-polarized component $\vec{p}$, whose polarization direction is lying in the incident plane, and s-polarized component $\vec{s}$, whose polarization direction is perpendicular to the incident plane (see Fig. 6). Recall that we've decomposed a ray emitted from the polarization field onto two orthogonal axes d_1 and d_2 as $\vec{E}_1$ and $\vec{E}_2$. We perform the s- and p-polarization decomposition for $\vec{E}_1$ and $\vec{E}_2$ separately:

$$\begin{aligned} \vec{s}_1 &= (\vec{E}_1 \cdot \vec{n}_{inci})\vec{n}_{inci} \\ \vec{s}_2 &= (\vec{E}_2 \cdot \vec{n}_{inci})\vec{n}_{inci} \end{aligned} \tag{11}$$

and

$$\begin{aligned} \vec{p}_1 &= \vec{E}_1 - \vec{s}_1 \\ \vec{p}_2 &= \vec{E}_2 - \vec{s}_2 \end{aligned} \tag{12}$$

We then superpose $\vec{s}_1$ with $\vec{s}_2$ and $\vec{p}_1$ with $\vec{p}_1$ to obtain the s- and p-polarized component of incident ray $\vec{i}$. Assume the phase difference between the s-polarized wave s and p-polarized wave p is δ (which is the same as the phase difference between $\vec{E}_1$ and $\vec{E}_2$). The amplitudes of the superposed waves for s- and p-polarized components [46] can be written as:

$$\begin{aligned} s &= \sqrt{(\| \vec{s}_1 \|^2 + \| \vec{s}_2 \|^2 + 2 \| \vec{s}_1 \| \| \vec{s}_2 \| \cos\delta)} \\ p &= \sqrt{(\| \vec{p}_1 \|^2 + \| \vec{p}_2 \|^2 + 2 \| \vec{p}_1 \| \| \vec{p}_2 \| \cos\delta)} \end{aligned} \tag{13}$$

Given the incident ray $\vec{i}$ and reflected ray $\vec{r}$, the reflection angle β_i can be written as:

$$\beta_i = \frac{1}{2} \cdot \arccos\left(\frac{(-\vec{i}) \cdot \vec{r}}{\| (-\vec{i}) \cdot \vec{r} \|}\right) \tag{14}$$

According to the Fresnel equations, the reflection rate of light is related to the polarization state, incident angle, and surface material (See Fig. 7). In particular, for $\vec{i}$, the strength of reflection or the reflectance coefficients of its p- and s-polarized components can be written as:

$$\begin{aligned} R_p(\beta_i, n_m) &= \left| \frac{n_{air}\sqrt{1 - (\frac{n_{air}}{n_m}\sin\beta_i)^2} - n_m \cos\beta_i}{n_{air}\sqrt{1 - (\frac{n_{air}}{n_m}\sin\beta_i)^2} + n_m \cos\beta_i} \right|^2 \\ R_s(\beta_i, n_m) &= \left| \frac{n_{air}\cos\beta_i - n_m\sqrt{1 - (\frac{n_{air}}{n_m}\sin\beta_i)^2}}{n_{air}\cos\beta_i + n_m\sqrt{1 - (\frac{n_{air}}{n_m}\sin\beta_i)^2}} \right|^2 \end{aligned} \tag{15}$$

where n_{air} is the refractive index of air (which can be approximated as one) and n_m is the refractive index of the surface, which is related to the surface material. It's worth noting that refractive indices of metal materials are complex numbers, which not only affect the relative amplitude, but also the phase shifts between p- and s-polarized components.

The amplitudes of p- and s- components of the reflection ray $\vec{r}$ can then be computed as $||R_s||s$ and $||R_p||p$. Therefore, the intensity of the reflection image can be obtained by combining the amplitude of s- and p- components of $\vec{r}$ because the intensity of a light is always the sum of intensities along two orthogonal directions of the light:

$$I(\nu_k) = \epsilon((||R_p||p)^2 + (||R_s||s)^2) \tag{16}$$

where ϵ is a scale factor that considers the absolute energy from the unpolarized backlight.

Eq. 16 models the reflection image under the polarization field with respect to the incident ray direction. Assume we know the refractive index n_m of the mirror surface. By capturing two reflection images $\hat{I}(\nu_k)$ at $k = 0$ ($\delta = 0$) and $k = 255$ ($\delta = \pi/2$), we can estimate the incident ray direction $\vec{i}$ and scale factor ϵ using the following objective function:

$$\arg\min_{\vec{i},\epsilon} \sum^{k=0,255} ||\hat{I}(\nu_k) - I(\nu_k)||^2 \qquad (17)$$

Eq. 17 can be solved by an iterative optimization using non-linear least square. In our implementation, we use the trust region reflective optimization algorithm, which is a Newton Step-based method that exhibits quadratical speed of convergence near the optimal value.

B. Ray-ray triangulation

After we obtain the incident rays $\vec{i}$, we can triangulate with the camera rays $\vec{r}$ to recover the mirror surface. Specifically, we estimate the surface normal by taking the half way vector between $\vec{i}$ and $\vec{r}$ as:

$$\vec{n} = \frac{\vec{r} - \vec{i}}{||\vec{r} - \vec{i}||} \qquad (18)$$

We then integrate the normal field using Poisson method to recover the 3D surface. In particular, we can model the surface as a height field $h(x, y)$, and represent normal vector at each point (x, y) using horizontal and vertical gradients as $(h_x, h_y, -1)$. When given the boundary condition (Neumann or Dirichlet) and the normal field, the problem of normal field integration to recover the 3D surface can be formulated to find the optimal surface z where:

$$\min_z \iint ((z_x - h_x)^2 + (z_y - h_y)^2)) dxdy \qquad (19)$$

Solving this optimization problem is equivalent to solving the Poisson equation: $\Delta z = h_{xx} + h_{yy}$, where Δ is the Laplacian operator: $\Delta = \partial^2/\partial x^2 + \partial^2/\partial y^2$.

VI. Experiments

In this section, we validate our approach on simulated and real surfaces. All experiments are performed on a PC with Intel i5-8600K CPU (6-Core 4.3GHz) and 16G memory using Matlab.

A. Simulated experiments

We perform simulation of our approach on a vase model. We implement a ray tracer to render the reflection images of polarization field based on our reflection image model.

In our simulation, we use a display with resolution 1920×1080 and the vase model is within a volume of $600 \times 300 \times 300$. We use the refractive index of silver (Ag) $n_m = 0.16 + 3.93i$ for the vase surface. We use perspective viewing camera with field of view $90°$ and resolution 1920×1080. We first establish pixel-point correspondences between the image and display by decoding a series of Gray Code reflection images. We then render two reflection images by displaying gray level $k = 0$ and $k = 255$ for estimating the incident ray direction. By triangulating the incident rays and camera rays, we recover the surface normal map and then recover the 3D surface using Poisson integration. The recovered normal map and 3D surface are shown in Fig. 8. We also compare our reconstructed normal map with the ground truth model and show the error map. The Root Mean Square (RMS) error of normal angles is $0.1481°$. This experiment shows that our approach produces highly accurate reconstruction.

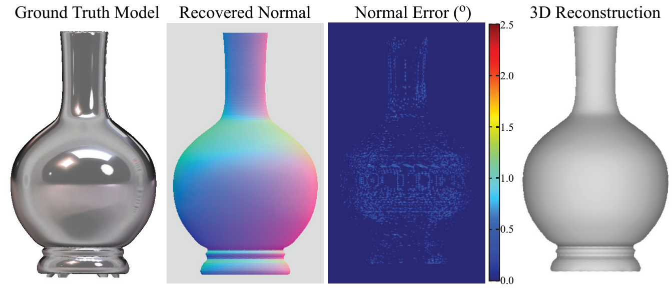

Fig. 8. Simulation experiment results on a vase model.

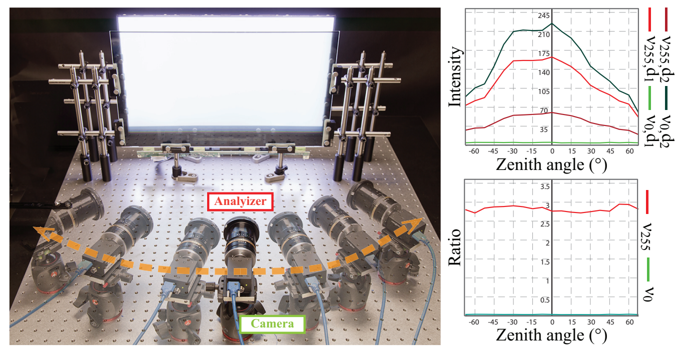

Fig. 9. Measuring the amplitude ratio γ from various viewing directions.

B. Real Experiments

We perform real experiments on various complex mirror objects to validate our approach. Our acquisition system is shown in Fig. 1. To generate the polarization field, we use a commercial IPS LCD monitor (Dell E2417H) and remove its top polarizer using acetone. We use a monochrome camera (PointGray GS3-U3-51S5M-C) with resolution 2448×2048 and focal length $50mm$ for capturing the reflection images of the polarization field from the mirror surface.

We first calibrate the acquisition system to establish a common coordinate for the display and the viewing camera. Since our viewing camera cannot cover the display in its field of view, we use an auxiliary camera to bridge the viewing camera and the display. The auxiliary camera is directly looking towards the display and share common field of view with the viewing camera. We mount a linear polarizer in the front to capture the displayed checkerboard as the top polarizer

Fig. 10. Real experiment results on three mirror objects.

of the LCD has been removed. Then the auxiliary camera and viewing camera are co-calibrated by checkerboard within the common view.

We also perform experiments to validate that the amplitude ratios γ are almost the same for different viewing angles. As shown in Fig. 9, we use a camera looking towards the display from different viewing angles (ranging from $-70°$ to $70°$ with a step of $7°$). We attach a linear polarizer (a.k.a analyzer) in front of the camera to capture horizontally and vertically polarized images. For each viewing angle, we capture images of gray level 255 and 0. We compute the ratio between intensities captured at $\vec{d1}$ and $\vec{d2}$ and plot the curves for both intensities and ratios at different viewing angles (see Fig. 9). This experiment demonstrates that we can use $\gamma(0, 0, \nu_k)$ to approximate $\gamma(\theta, \phi, \nu_k)$ of arbitrary ray directions for the same intensity level k. Note that $\gamma(0, 0, \nu_0)$ and $\gamma(0, 0, \nu_{255})$ are used in our optimization (Eq.17) for estimating the incident ray.

In order to obtain the incident plane, we first need to determine the origins of incident rays. We use Gray Code to establish pixel-point correspondences and decode ray positions. Since our display is with resolution 1920×1080, we use 22 patterns to resolve all pixels. Since the captured intensity varies with polarization states and surface geometry, we compare the capture reflection images with the all-white and all-black images to robustly decode the Gray Code. After we have the ray positions P_{disp}, we can apply our reflection image formation model to estimate the incident ray directions. Finally we triangulate the incident rays with reflected ray for surface reconstruction.

We perform experiments on three real mirror objects (buddha, horse and cat). These objects are with various sizes. The horse and buddha is around $100mm \times 100mm \times 200mm$ and cat is around $30mm \times 50mm \times 100mm$. These objects are made of Nickel (Ni) with refractive index $n_m = 1.96 + 3.84i$. All three objects are placed around $10cm$ in front of the display. Our reconstruction results are shown in 10. For each object, we demonstrate the real photograph of the object, captured images at gray level 0 (red) and 255 (green), reconstructed normal map and 3D surfaces. It is worth noting that the cat eye is concave while our approach still produces reliable reconstruction.

VII. Conclusions and Discussions

In this paper, we have presented an approach for reconstructing complex mirror surfaces using polarization field, which is generated by a commercial LCD without top polarizer. We have shown that the angular information embedded in the polarization field can effectively resolve ambiguities in mirror surface reconstruction. To recover mirror surfaces, we have derived an image formation model under the polarization field and developed an optimization algorithm for estimating the incident ray. Comprehensive experiments on simulated and real surfaces have demonstrated the effectiveness of our approach.

One limitation of our approach is that we assume the reflection only occurs once on the mirror surface and thus cannot deal with interreflection. Derive a reflection model with multiple reflections could be an interesting future direction. Second, our approach still needs to use the Gray Code to establish pixel correspondences. In the future we plan to design more efficient coding scheme and integrate with the polarization field. In this paper, we demonstrate using the polarization field for mirror surface reconstruction. It is possible to extend it for more general objects thus resulting in new 3D reconstruction methods.

Acknowledgment

This work was partially supported by the Louisiana Board of Regents under Grant LEQSF(2018-21)-RD-A-10.

References

[1] J. Balzer, S. Hofer, and J. Beyerer, "Multiview specular stereo reconstruction of large mirror surfaces," in *Computer Vision and Pattern Recognition (CVPR)*, 2011. 1, 2

[2] J. Balzer, D. Acevedo-Feliz, S. Soatto, S. Höfer, M. Hadwiger, and J. Beyerer, "Cavlectometry: Towards holistic reconstruction of large mirror objects," in *International Conference on 3D Vision (3DV)*, 2014. 1, 2

[3] M. Weinmann, A. Osep, R. Ruiters, and R. Klein, "Multi-view normal field integration for 3d reconstruction of mirroring objects," in *International Conference on Computer Vision (ICCV)*, 2013. 1, 2

[4] K. N. Kutulakos and E. Steger, "A theory of refractive and specular 3d shape by light-path triangulation," *International Journal of Computer Vision*, vol. 76, no. 1, pp. 13–29, 2008. 1, 2

[5] K. Ikeuchi, "Determining surface orientations of specular surfaces by using the photometric stereo method," *IEEE Transactions on Pattern Analysis and Machine Intelligence*, no. 6, pp. 661–669, 1981. 1, 2

[6] S. Savarese and P. Perona, "Local analysis for 3d reconstruction of specular surfaces?part ii," in *European Conference on Computer Vision (ECCV)*, 2002. 1, 2

[7] M. Tarini, H. P. Lensch, M. Goesele, and H.-P. Seidel, "3d acquisition of mirroring objects using striped patterns," *Graphical Models*, vol. 67, no. 4, pp. 233–259, 2005. 1, 2

[8] D. Lanman, G. Wetzstein, M. Hirsch, W. Heidrich, and R. Raskar, "Polarization fields: dynamic light field display using multi-layer lcds," *ACM Transactions on Graphics*, vol. 30, no. 6, pp. 186–186, 2011. 1

[9] R. W. Fleming, A. Torralba, and E. H. Adelson, "Specular reflections and the perception of shape," *Journal of Vision*, vol. 4, no. 9, pp. 10–10, 2004. 2

[10] S. Savarese, L. Fei-Fei, and P. Perona, "What do reflections tell us about the shape of a mirror?" in *Symposium on Applied Perception in Graphics and Visualization*, 2004. 2

[11] T. Bonfort and P. Sturm, "Voxel carving for specular surfaces," in *International Conference on Computer Vision (ICCV)*, 2003. 2

[12] Y. Ding, J. Yu, and P. Sturm, "Recovering specular surfaces using curved line images," in *Computer Vision and Pattern Recognition (CVPR)*, 2009. 2

[13] B. Jacquet, C. Hane, K. Koser, and M. Pollefeys, "Real-world normal map capture for nearly flat reflective surfaces," in *International Conference on Computer Vision (ICCV)*, 2013. 2

[14] R. Swaminathan, M. D. Grossberg, and S. K. Nayar, "A perspective on distortions," in *Computer Vision and Pattern Recognition (CVPR)*, 2003. 2

[15] T. Chen, M. Goesele, and H.-P. Seidel, "Mesostructure from specularity," in *Computer Vision and Pattern Recognition (CVPR)*, 2006. 2

[16] S. K. Nayar, A. C. Sanderson, L. E. Weiss, and D. A. Simon, "Specular surface inspection using structured highlight and gaussian images," *IEEE Transactions on Robotics and Automation*, vol. 6, no. 2, pp. 208–218, 1990. 2

[17] M. Oren and S. K. Nayar, "A theory of specular surface geometry," *International Journal of Computer Vision*, vol. 24, no. 2, pp. 105–124, 1997. 2

[18] A. S. Sanderson, L. E. Weiss, and S. K. Nayar, "Structured highlight inspection of specular surfaces," *IEEE Transactions on Pattern Analysis and Machine Intelligence*, no. 1, pp. 44–55, 1988. 2

[19] S. Roth and M. J. Black, "Specular flow and the recovery of surface structure," in *Computer Vision and Pattern Recognition (CVPR)*, 2006. 2

[20] Y. Adato, Y. Vasilyev, O. Ben-Shahar, and T. Zickler, "Toward a theory of shape from specular flow," in *International Conference on Computer Vision (ICCV)*, 2007. 2

[21] A. C. Sankaranarayanan, A. Veeraraghavan, O. Tuzel, and A. Agrawal, "Specular surface reconstruction from sparse reflection correspondences," in *Computer Vision and Pattern Recognition (CVPR)*, 2010. 2

[22] A. Veeraraghavan, O. Tuzel, A. Agrawal *et al.*, "Image invariants for smooth reflective surfaces," in *European Conference on Computer Vision (ECCV)*, 2010. 2

[23] C. Godard, P. Hedman, W. Li, and G. J. Brostow, "Multi-view reconstruction of highly specular surfaces in uncontrolled environments," in *International Conference on 3D Vision (3DV)*, 2015. 2

[24] Y. Francken, T. Cuypers, T. Mertens, J. Gielis, and P. Bekaert, "High quality mesostructure acquisition using specularities," in *Computer Vision and Pattern Recognition (CVPR)*, 2008. 2

[25] N. J. Morris and K. N. Kutulakos, "Reconstructing the surface of inhomogeneous transparent scenes by scatter-trace photography," in *International Conference on Computer Vision (ICCV)*, 2007. 2

[26] M. D. Grossberg and S. K. Nayar, "The raxel imaging model and ray-based calibration," *International Journal of Computer Vision*, vol. 61, no. 2, pp. 119–137, 2005. 2

[27] B. Wu, Y. Zhou, Y. Qian, M. Gong, and H. Huang, "Full 3D reconstruction of transparent objects," *ACM Transactions on Graphics (Proceedings of SIGGRAPH)*, vol. 37, no. 4, pp. 103:1–103:11, 2018. 2

[28] M. Liu, K.-Y. K. Wong, Z. Dai, and Z. Chen, "Specular surface recovery from reflections of a planar pattern undergoing an unknown pure translation," in *Asian Conference on Computer Vision (ACCV)*, 2010. 2

[29] V. Chari and P. Sturm, "A theory of refractive photo-light-path triangulation," in *Computer Vision and Pattern Recognition (CVPR)*, 2013. 2

[30] D. Liu, X. Chen, and Y.-H. Yang, "Frequency-based 3d reconstruction of transparent and specular objects," in *Conference on Computer Vision and Pattern Recognition (CVPR)*, 2014. 2

[31] D. Miyazaki, R. T. Tan, K. Hara, and K. Ikeuchi, "Polarization-based inverse rendering from a single view," in *International Conference on Computer Vision (ICCV)*, 2003. 2

[32] O. Morel, F. Meriaudeau, C. Stolz, and P. Gorria, "Polarization imaging applied to 3d reconstruction of specular metallic surfaces," in *Machine Vision Applications in Industrial Inspection XIII*, vol. 5679. International Society for Optics and Photonics, 2005, pp. 178–187. 2

[33] G. A. Atkinson and E. R. Hancock, "Recovery of surface orientation from diffuse polarization," *IEEE Transactions on Image Processing*, vol. 15, no. 6, pp. 1653–1664, 2006. 2

[34] A. H. Mahmoud, M. T. El-Melegy, and A. A. Farag, "Direct method for shape recovery from polarization and shading," in *International Conference on Image Processing (ICIP)*, 2012. 2

[35] W. A. Smith, R. Ramamoorthi, and S. Tozza, "Linear depth estimation from an uncalibrated, monocular polarisation image," in *European Conference on Computer Vision (ECCV)*, 2016. 2

[36] O. Drbohlav and R. Sara, "Unambiguous determination of shape from photometric stereo with unknown light sources," in *International Conference on Computer Visio (ICCV)*, 2001. 2

[37] T. Ngo Thanh, H. Nagahara, and R.-i. Taniguchi, "Shape and light directions from shading and polarization," in *Computer Vision and Pattern Recognition (CVPR)*, 2015. 2

[38] C. P. Huynh, A. Robles-Kelly, and E. Hancock, "Shape and refractive index recovery from single-view polarisation images," in *Computer Vision and Pattern Recognition (CVPR)*, 2010. 2

[39] G. A. Atkinson and E. R. Hancock, "Multi-view surface reconstruction using polarization," in *International Conference of Computer Vision (ICCV)*, 2005. 2

[40] D. Miyazaki, M. Kagesawa, and K. Ikeuchi, "Transparent surface modeling from a pair of polarization images," *IEEE Transactions on Pattern Analysis & Machine Intelligence*, no. 1, pp. 73–82, 2004. 2

[41] S. Rahmann and N. Canterakis, "Reconstruction of specular surfaces using polarization imaging," in *Computer Vision and Pattern Recognition (CVPR)*, 2001. 2

[42] D. Miyazaki, T. Shigetomi, M. Baba, R. Furukawa, S. Hiura, and N. Asada, "Polarization-based surface normal estimation of black specular objects from multiple viewpoints," in *3D Imaging, Modeling, Processing, Visualization and Transmission (3DIMPVT)*, 2012. 2

[43] Z. Cui, J. Gu, B. Shi, P. Tan, and J. Kautz, "Polarimetric multi-view stereo," in *Computer Vision and Pattern Recognition (CVPR)*, 2017. 2

[44] A. Kadambi, V. Taamazyan, B. Shi, and R. Raskar, "Polarized 3d: High-quality depth sensing with polarization cues," in *International Conference on Computer Vision (ICCV)*, 2015. 2

[45] P. Yeh and C. Gu, *Optics of liquid crystal displays*. John Wiley & Sons, 2010. 3

[46] R. P. Feynman, R. B. Leighton, and M. Sands, *The Feynman lectures on physics, Vol. I*. Addison Wesley, 2010. 5